The *Herschel* M 33 extended survey (HerM33es): PACS spectroscopy of the star-forming region BCLMP 302[⋆]

B. Mookerjea[1], C. Kramer[2], C. Buchbender[2], M. Boquien[3], S. Verley[4], M. Relaño[4], G. Quintana-Lacaci[2], S. Aalto[5], J. Braine[6], D. Calzetti[3], F. Combes[7], S. Garcia-Burillo[8], P. Gratier[6], C. Henkel[9], F. Israel[10], S. Lord,[11], T. Nikola[12], M. Röllig[13], G. Stacey[12], F. S. Tabatabaei[9], F. van der Tak[15], and P. van der Werf[10,16]

[1] Tata Institute of Fundamental Research, Homi Bhabha Road, Mumbai 400005, India
  e-mail: bhaswati@tifr.res.in
[2] Instituto Radioastronomía Milimétrica, Av. Divina Pastora 7, Nucleo Central, 18012 Granada, Spain
[3] University of Massachusetts, Department of Astronomy, LGRT-B 619E, Amherst, MA 01003, USA
[4] Universidad de Granada, 18012 Granada, Spain
[5] Department of Radio and Space Science, Onsala Observatory, Chalmers University of Technology, 43992 Onsala, Sweden
[6] Laboratoire d'Astrophysique de Bordeaux, Université Bordeaux 1, Observatoire de Bordeaux, OASU, UMR 5804, CNRS/INSU, BP 89, Floirac 33270, France
[7] Observatoire de Paris, LERMA, CNRS, 61 Av. de l'Observatoire, 75014 Paris, France
[8] Observatorio Astronómico Nacional (OAN) – Observatorio de Madrid, Alfonso XII 3, 28014 Madrid, Spain
[9] Max Planck Institut für Radioastronomie, Auf dem Hügel 69, 53121 Bonn, Germany
[10] Leiden Observatory, Leiden University, PO Box 9513, 2300 RA Leiden, The Netherlands
[11] IPAC, MS 100-22 California Institute of Technology, Pasadena, CA 91125, USA
[12] Department of Astronomy, Cornell University, Ithaca, NY 14853, USA
[13] KOSMA, I. Physikalisches Institut, Universität zu Köln, Zülpicher Strasse 77, 50937 Köln, Germany
[14] Institute of Astronomy, University of Cambridge, Madingley Road, Cambridge CB3 0HA, UK
[15] SRON Netherlands Institute for Space Research, Landleven 12, 9747 AD Groningen, The Netherlands
[16] SUPA, Institute for Astronomy, University of Edinburgh, Royal Observatory, Blackford Hill, Edinburgh EH9 3HJ 7, UK

ABSTRACT

Context. The emission line of [C II] at $158\,\mu m$ is one of the strongest cooling lines of the interstellar medium (ISM) in galaxies.
Aims. Distinguishing the relative contributions of the different ISM phases to [C II] emission is a major objective of the HerM33es program, a *Herschel* key project to study the ISM in the nearby spiral galaxy M 33.
Methods. Using PACS, we have mapped the emission of [C II] $158\,\mu m$, [O I] $63\,\mu m$, and other FIR lines in a $2' \times 2'$ region of the northern spiral arm of M 33, centered on the H II region BCLMP 302. At the peak of Hα emission, we observed in addition a velocity-resolved [C II] spectrum using HIFI. We use scatterplots to compare these data with PACS $160\,\mu m$ continuum maps, and with maps of CO and H I data, at a common resolution of $12''$ or 50 pc. Maps of Hα and $24\,\mu m$ emission observed with Spitzer are used to estimate the SFR. We created maps of the [C II] and [O I] $63\,\mu m$ emission and detected [N II] $122\,\mu m$ and [N III] $57\,\mu m$ at individual positions.
Results. The [C II] line observed with HIFI is significantly broader than that of CO, and slightly blue-shifted. In addition, there is little spatial correlation between [C II] observed with PACS and CO over the mapped region. There is even less spatial correlation between [C II] and the atomic gas traced by H I. Detailed comparison of the observed intensities towards the H II region with models of photo-ionization and photon-dominated regions, confirms that a significant fraction, 20–30%, of the observed [C II] emission stems from the ionized gas and not from the molecular cloud. The gas heating efficiency, using the ratio of [C II] to the TIR as a proxy, varies between 0.07 and 1.5%, with the largest variations found outside the H II region.

Key words. galaxies: individual: M 33 – photon-dominated region (PDR) – HII regions – Local Group – galaxies: ISM – galaxies: star formation

1. Introduction

The thermal balance and dynamics of the interstellar medium in galaxies, is best studied through spectroscopic observations of its major cooling lines: [C I], [C II], and [O I] trace the transition regions between the atomic and molecular gas, while CO traces the dense molecular gas that provides the reservoir for stars to form. Most of the important cooling lines lie in the far-infrared and submillimeter regime. Therefore, it is difficult or impossible to study them with ground-based telescopes, while previous space-based telescopes provided low sensitivity and coarse angular resolution. The infrared line emission is mostly optically thin and can be traced throughout the densest regions in galaxies, allowing an unhindered view of the ISM. *Herschel* provides, for the first time, an opportunity to image the major tracers of the ISM at a sensitivity, and spectral and spatial resolutions that allow us to study the interplay between star formation and the active ISM throughout our Milky Way and in nearby galaxies.

The two fine structure lines of [C II] at $158\,\mu m$ and [O I] at $63\,\mu m$, are the strongest cooling lines of the ISM, carrying up to a few percent of the total energy emitted from galaxies at far-infrared wavelengths. The [C II] line lies 92 K above the ground state with a critical density for collisions with H of $3 \times 10^3\,cm^{-3}$

([Kaufman et al. 1999](#)). While both lines are thought to trace photon-dominated regions (PDRs) at the FUV-irradiated surfaces of molecular clouds, it was realized early-on that a non-negligible fraction of the [C II] emission may stem from the ionized medium ([Heiles 1994](#)). Owing to its higher upper energy level (228 K) and higher critical density of $\simeq 5 \times 10^5$ cm^{-3}, the [O I] 63 μm line is a more dominant coolant in warmer and denser neutral regions (e.g. [Röllig et al. 2006](#)).

The [C II] and the [O I] lines are diagnostics that help us to infer the physical conditions in the gas, its temperatures, densities, and radiation fields, by comparing the intensities and their ratios with predictions of PDR models (e.g., [Tielens & Hollenbach 1985](#); [Wolfire et al. 1990](#); [Kaufman et al. 1999](#); [Röllig et al. 2007](#); [Ferland et al. 1998](#)). Previous observational studies of [C II] emission from external galaxies include the statistical studies by [Crawford et al. (1985)](#), [Stacey et al. (1991)](#), and [Malhotra et al. (2001)](#). More recently, the [C II] emission from a few individual galaxies e.g., LMC ([Israel et al. 1996](#)), M 51 ([Nikola et al. 2001](#); [Kramer et al. 2005](#)), NGC 6946 ([Madden et al. 1993](#); [Contursi et al. 2002](#)), M 83 ([Kramer et al. 2005](#)), NGC 1313 ([Contursi et al. 2002](#)), M 31 ([Rodriguez-Fernandez et al. 2006](#)), and NGC1097 ([Contursi et al. 2002](#); [Beirão et al. 2010](#)) has been observed. These papers explore the origin of the [C II] emission. The study of LMC by [Israel et al. (1996)](#) was at a resolution of 16 pc and [Rodriguez-Fernandez et al. (2006)](#) resolved the spiral arms of M 31 on spatial scales of 300 pc.

In addition to [C II] and [O I] 63 μm, there are several additional FIR lines, the mid-J CO transitions, and lines of single and double ionized N and O, which provide information about the gas density (multiple transitions of the same ions), hardness of the stellar radiation field (ratio of the intensities of two ionization states of the same species), and ionizing flux. In particular, the [N II] lines at 122 μm and 205 μm allow us to estimate the density of the ionized gas, which is a key parameter in modeling the [C II] emission originating from the ionized gas.

Although much detailed information can be obtained by studying nearby (Milky Way) sites of star formation, a more comprehensive insight can be obtained by targeting a nearby moderately inclined galaxy such as M 33. M 33 is a nearby, moderately metal-poor late-type spiral galaxy with no bulge or ring, classified as SA(s)cd. It is the third largest member of the Local Group. Its mass, size, and average metallicity are similar to those of the Large Magellanic Cloud (LMC). M 33 hosts some of the brightest H II complexes in the Local Group. NGC 604 is the second brightest H II region after 30 Doradus in the LMC. Its inclination ($i = 56°$) ([Regan & Vogel 1994](#)) yields a small line-of-sight depth, which allows us to study individual cloud complexes that are unaffected by distance ambiguities and confusion similar to those influencing Galactic observations. Its close distance of 840 kpc ([Freedman et al. 1991](#)) provides a spatial resolution of 50 pc at 12″, allowing us to resolve giant molecular associations in its disk with current single-dish millimeter and far-infrared telescopes such as the IRAM 30 m telescope and *Herschel*. Its recent star formation activity, together with the absence of signs of recent mergers, make M 33 an ideal target to study the interplay of gas, dust, and star formation in its disk. This is the aim of the open time key program "*Herschel* M 33 extended survey" HerM33es ([Kramer et al. 2010](#)). To this end, we are surveying the major cooling lines, notably [C II], [O I], and [N II], as well as the dust spectral energy distribution (SED) using all three instruments onboard *Herschel*, HIFI, PACS, and SPIRE. We also use ancillary observations of Hα, H I, CO, and dust continuum at 24 μm. The HerM33es PACS and HIFI spectral line observations
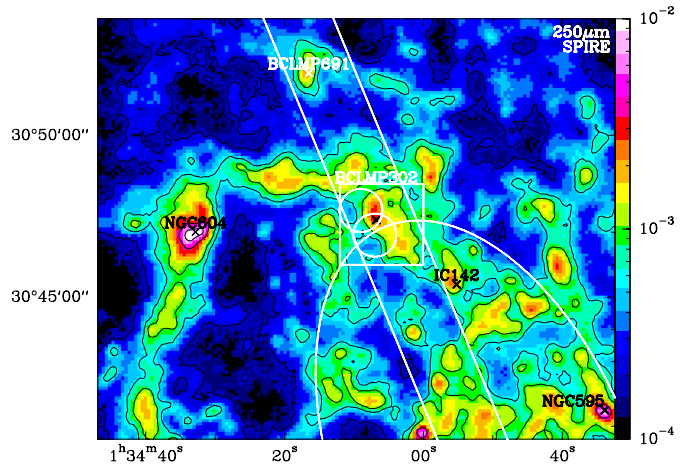

Fig. 1. 250 μm *Herschel*-SPIRE dust continuum image of the northern spiral arm of M 33 along with the locations of the prominent H II regions NGC 604, NGC 595, IC 142, BCLMP 302, and BCLMP 691. The rectangle delineates the area observed with PACS and HIFI, which is centered on BCLMP 302. The white circles indicate the positions and 70″ beam of ISO/LWS observations done within the BCLMP 302 region. The white ellipse delineates 2 kpc galactocentric distance. The two parallel lines running along the major axis of M 33, mark the strip for which we plan to observe the [C II] and other FIR lines using PACS and HIFI.

will focus on a number of individual regions along the major axis of M 33, which will initially be presented individually.

Here, we present first spectroscopic results obtained for BCLMP302, one of the brightest H II regions of M 33. We discuss a 2′ × 2′ ($\sim$0.5 kpc × 0.5 kpc) field in the northern spiral arm at a galactocentric distance of 2 kpc (Fig. 1). This region lies along the major axis of M 33, and houses one of the brightest H II regions, BCLMP 302 ([Boulesteix et al. 1974](#); [Israel & van der Kruit 1974](#)). Using ISO/SWS, [Willner & Nelson-Patel (2002)](#) studied the neon abundances of H II regions in M 33, including BCLMP 302. [Rubin et al. (2008)](#) used *Spitzer*-IRS to map the emission lines of [S IV] 10.51, H(7–6) 12.37, [Ne II] 12.8, [Ne III] 15.56, and [S III] 18.71 μm in 25 H II regions in M 33, including BCLMP 302. ISO/LWS [C II] unresolved spectra at $\sim$70″ resolution ([Gry et al. 2003](#)) are available for this region from the archive. Here, we present PACS maps of [C II] and [O I] 63 μm at a resolution of 12″, together with a HIFI [C II] spectrum of 0.63 km s^{-1} velocity resolution. We compare these data with: (i) the Hα emission tracing the ionized gas; (ii) dust continuum images at mid- and far-infrared wavelengths observed with *Spitzer* and *Herschel*, tracing the dust heated by newly formed stars and the diffuse interstellar radiation field; and (iii) CO and H I emission tracing the neutral molecular and atomic gas.

The rest of the paper is organized as follows: Sect. 2 presents details of our observations and ancillary data, Sect. 3 states the basic results of the spectroscopic observations and both a qualitative and a quantitative comparison of the [C II] and [O I] emission with all other available tracers and their correlations. Section 4 studies the role of [C II] as an indicator of the star formation rate (SFR) and Sect. 5 analyzes the energy balance in the mapped region. Section 6 presents a detailed analysis of the emission from the Hα peak position in BCLMP 302 in terms of models of PDRs. In Sect. 7, we summarize and discuss the major findings of the paper.
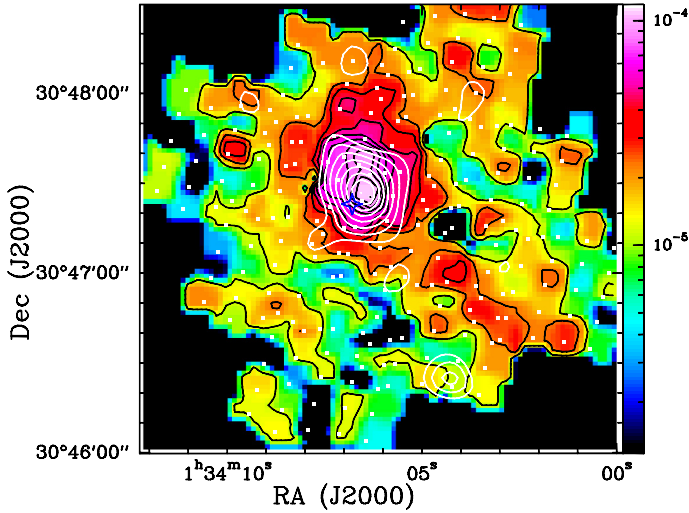
Fig. 2. Maps of 158 μm [C II] (in color and black contours) and 63 μm [O I] (white contours) emission observed with PACS toward BCLMP 302. The [C II] intensities shown in the color wedge are in units of erg s^{-1} cm^2 sr^{-1}. The [O I] 63 μm map has been smoothed to 12″ for easy comparison with [C II]. The Hα peak observed with HIFI is marked with the asterisk. The white dots show the footprint of the PACS observations. The contour levels are from 10% to 100% (in steps of 10%) of peak [C II] intensity of 1.18×10^{-4} erg cm^{-2} s^{-1} sr^{-1}. The contour levels for [O I] 63 μm emission are from 30% to 100% (in steps of 10%) of the peak of 3.0×10^{-5} erg cm^{-2} s^{-1} sr^{-1}. Both images are at a common resolution of 12″.

2. Observations

2.1. Herschel: PACS mapping

A region extending over 2′×2′ around the H II region BCLMP 302 in the northern arm of M 33 was observed with the 5 × 5 pixel integral field unit (IFU) of the PACS Spectrometer using the wavelength switching (WS) mode in combination with observations of an emission-free off-source position outside of the galaxy at RA/Dec (J2000) = 22.5871°/30.6404°. The field of view of the IFU is 47″ × 47″ with 9.″4 pixels (Poglitsch et al. 2010). We used the first and third order gratings to observe the [C II] 157.7 μm, [O I] 63.18 μm, [O I] 145.52 μm, [N II] 121.9 μm, [N III] 57.3 μm, and [N II] 205.18 μm lines, with the shortest possible observing time (1 line repetition, 1 cycle), and with a reference position at RA = 01^{h}30^{m}20.9, Dec = 30°38′25.″4 (J2000). The reference position was selected based on H I and 100 μm ISSA[1] maps.

For all the lines, a 3 × 3 raster was observed on a 40″ grid with the IFU centered at RA = 01^{h}34^{m}05.9 Dec = +30°47′18.″6 (J2000) with position angle, PA = 22.5°. The resulting footprint is shown in Fig. 2. The *FWHM* beam size of the PACS spectrometer is 9.2″ near 63 μm and 11.2″ near 158 μm (Sturm, priv. comm.). The lines are unresolved, as the spectral resolution of PACS is larger than 90 km s^{-1} for all lines. The observations were performed on January 7, 2010 and the total observing time was 1.1 h for all the six lines. The PACS spectra were reduced using HIPE version 3.0 CIB 1452 (Ott et al. 2010). The WS data reduction pipeline was custom-made by the NASA *Herschel* Science Center (NHSC) helpdesk. The data were exported to FITS datacubes, which were later analyzed using internally developed IDL routines to extract the line intensity maps.

---
[1] IRAS Sky Survey Atlas.
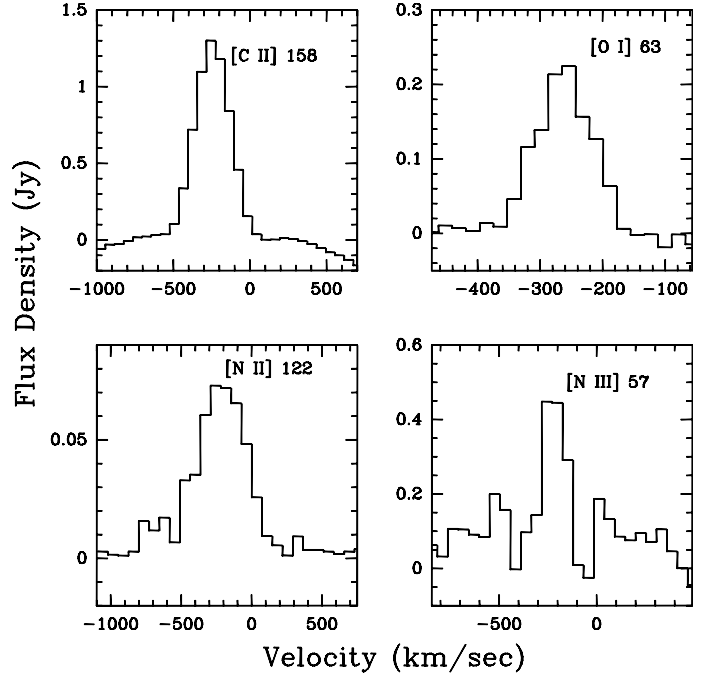
Fig. 3. PACS spectra of [C II] (158 μm), [O I] (63 μm), [N II] (122 μm) and [N III] 57 μm at the Hα peak position of BCLMP 302. The LSR velocity is given. All lines are unresolved, i.e. line profiles only reflect the instrumental profiles.

Table 1. Peak, signal-to-noise ratio (S/N), and sigma values of the integrated line intensities at the Hα peak position for the lines detected with PACS all at original resolution.

Line	Peak (S/N)	1σ
	erg s^{-1} cm^{-2} sr^{-1}	erg s^{-1} cm^{-2} sr^{-1}
[C II] 158 μm	1.18×10^{-4} (67)	1.72×10^{-6}
[O I] 63 μm	7.20×10^{-5} (6)	1.20×10^{-5}
[N II] 122 μm	9.95×10^{-6} (7)	1.42×10^{-6}
[N III] 57 μm	1.30×10^{-5} (7)	1.80×10^{-6}

Using PACS, the [C II]158 μm, [O I] 63 μm, [N II] 122 μm, and the [N III] 57 μm lines were detected. The lines of [O I] 145 μm and the [N II] 205 μm were not detected. The peak and 1σ noise limits of the intensities of the [C II], [O I], [N II] 122 μm, and [N III] 57 μm lines in the spectra, at the Hα peak position, are presented in Table 1. Figure 3 show the observed PACS spectra at the position of the Hα peak position. The peak integrated intensities were derived by first fitting and subtracting a polynomial baseline of second order and then fitting a Gaussian. Owing to the unequal coverage of different positions, as seen from the grid of observed positions shown in Fig. 2, the rms measured is not uniform, but varies by about a factor of three over the entire map.

2.2. Herschel: HIFI spectrum at the Hα peak

Using HIFI, we observed a single spectrum at the peak position (RA = 01^{h}34^{m}06.79 Dec = 30°47′23.″1 (J2000)) of the Hα emission from BCLMP 302 (Fig. 4). The HIFI spectrum was taken on 01 August 2010 during one hour of observing time using the load chop mode with the same reference position as used for the PACS observation. The frequency of the [C II] line is 1 900 536.9 MHz, known to within an uncertainty of 1.3 MHz
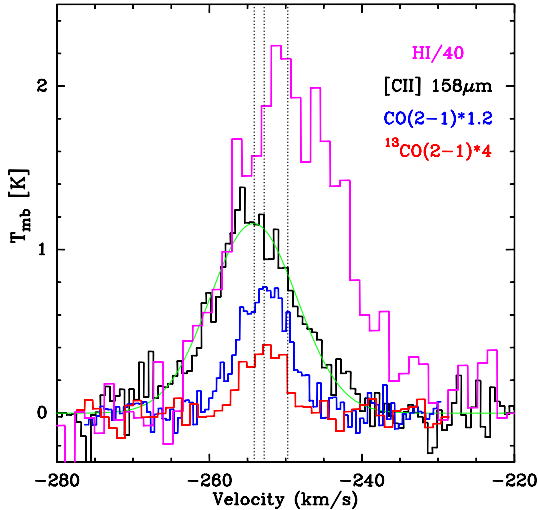
Fig. 4. All four spectra of [C II], H I, and the (2–1) transition of CO and ^{13}CO at the Hα peak position of the H II region BCLMP 302. All four spectra are at ~12″ resolution allowing for a detailed comparison. The vertical lines denote the velocities –249.7, –252.8, and –254.1 km s^{-1} corresponding to H I, CO, and [C II] emission, respectively.

(0.2 km s^{-1}) (Cooksy et al. 1986). The blue-shifted line required the local oscillator to be tuned to 1899.268 GHz, about the highest frequency accessible to HIFI. The [C II] spectra were recorded using the wide-band acousto optical spectrometer, covering a bandwidth of 2.4 GHz for each polarization with a spectral resolution of 1 MHz. We calculated the noise-weighted averaged spectrum, combining both polarizations. A fringe fitting tool available within HIPE was used to subtract standing waves, subsequently the data were exported to CLASS for further analysis. A linear baseline was next subtracted and the spectrum was rebinned to a velocity resolution of 0.63 km s^{-1} (Fig. 4). We scaled the resulting data to the main beam scale assuming a beam efficiency of 69%, and used the Ruze formula with the beam efficiency for a perfect primary mirror being given by $\eta_{\rm mb,0} = 0.76$ and a surface accuracy of $\sigma = 3.8\,\mu$m (Olberg 2010). The measured peak temperature from a Gaussian fit is 1.14 K and the rms (1σ limit) is 110 mK at 0.63 km s^{-1} resolution, which is consistent to within 10% of the rms predicted by HSPOT. The half power beam width (HPBW) is 12.2″.

2.3. IRAM 30 m CO observations

For comparison with the [C II] spectrum, we observed spectra of the (2–1) and (1–0) transitions of ^{12}CO and ^{13}CO, at the position of the Hα peak, using the IRAM 30 m telescope on 21 August 2010. These observations used the backend VESPA. The spectra were smoothed to a velocity resolution of 1 km s^{-1} for all the CO lines. The forward and beam efficiencies are 95% and 80%, respectively, for the (1–0) transition. The same quantities are 90% and 58% for the (2–1) transition. The half-power beam widths for the (1–0) and (2–1) transitions are 22″ and 12″, respectively.

2.4. Complementary data for comparison

We compare the *Herschel* data of the BCLMP 302 region, with the H I VLA and CO(2–1) HERA/30 m map at 12″ resolution presented by Gratier et al. (2010), to which we refer for a presentation of the noise properties.

We also use the *Spitzer* MIPS 24 μm map presented by Tabatabaei et al. (2007), the KPNO Hα map (Hoopes & Walterbos 2000), and the HerM33es PACS and SPIRE maps at 100, 160, 250, 350, and 500 μm (Kramer et al. 2010; Verley et al. 2010; Boquien et al. 2010). The angular resolution of the 100 and 160 μm PACS maps are ~6″ and 12″. The rms noise levels of the PACS maps are 2.6 mJy pix^{-2} at 100 μm and 6.9 mJy pix^{-1} at 160 μm where the pixel sizes are 3.″2 and 6.″4, respectively.

The [C II] observations at two positions within our mapped region were extracted from the ISO/LWS archival data. The two positions are at RA = 01$^{\rm h}$34$^{\rm m}$07$^{\rm s}$ Dec = 30°46′55″ (J2000) and RA = 01$^{\rm h}$34$^{\rm m}$09$^{\rm s}$ Dec = 30°47′41″ (J2000).

3. Results

3.1. PACS far-infrared spectroscopy

Within the 2′ × 2′ region mapped with PACS (Fig. 2), we detected extended [C II] emission from (a) the northern spiral arm traced e.g. by the 100 μm emission, with the strongest emission arising towards the H II region BCLMP 302 and (b) from the diffuse regions to the south-east and north-west. Comparison of the [C II] PACS intensities with the ISO/LWS [C II] data at the two positions shows an agreement of better than 11% at both positions. For the comparison of the intensities at the LWS positions, we first convolved the PACS [C II] map to the angular resolution of the LWS data. The full ISO/LWS [C II] data set along the major axis of M 33 will be published in a separate paper by Abreu et al. (in prep.).

Some of the PACS [O I] 63 μm spectra displayed baseline problems, attributed to the now decommissioned wavelength switching mode. Spectra taken along the [C II] emitting part of the spiral arm extending north-east to south-west showed problems and were blanked out. Both the [N II] 122 μm and the [N III] 57 μm lines were detected at only a few positions within the mapped region. The maps of [O I] 63 μm and [C II] 158 μm emission towards the H II region look very similar and both peak at RA = 01$^{\rm h}$34$^{\rm m}$ 06.$^{\rm s}$3, Dec = 30°47′25.″30. In addition, the [O I] 63 μm map shows a secondary peak towards the southwest, to the south of the [C II] ridge, at RA = 01$^{\rm h}$34$^{\rm m}$04.$^{\rm s}$364 Dec = 30°46′26.″55 (J2000), which is not found in the [C II] map. The second [O I] peak lies between the two ridges detected in CO(2–1) and coincides with an H I peak. This suggests that the [O I] emission at this peak position arises in very dense atomic gas.

Overlays of the [C II] map with maps of Hα, H I, CO(2–1), and dust continuum in the MIR and FIR (MIPS 24 μm, PACS 100 and 160 μm) are shown in Fig. 5. The dust continuum maps correlate well with the [C II] map. They peak towards the H II region and show the spiral arm extending from the H II region in the south-western direction. In contrast, CO emission displays a clumpy structure wrapping around the H II region towards the east. CO emission shows the spiral arm seen in the continuum, but its peaks are shifted towards the south. The H I emission shows a completely different morphology, peaking towards the north and south of the H II region and showing a clumpy filament running towards the west. Further below, we discuss the correlations in more detail.

Figure 6 shows overlays of the [O I] 63 μm map at a resolution of 12″ with H I and CO(2–1). Towards the south and south-west of the H II region, the [O I] 63 μm emission matches the H I emission well. This is surprising given the high excitation requirements for the [O I] line. The secondary [O I] 63 μm peak towards the south-west, is also traced by H I. It lies between
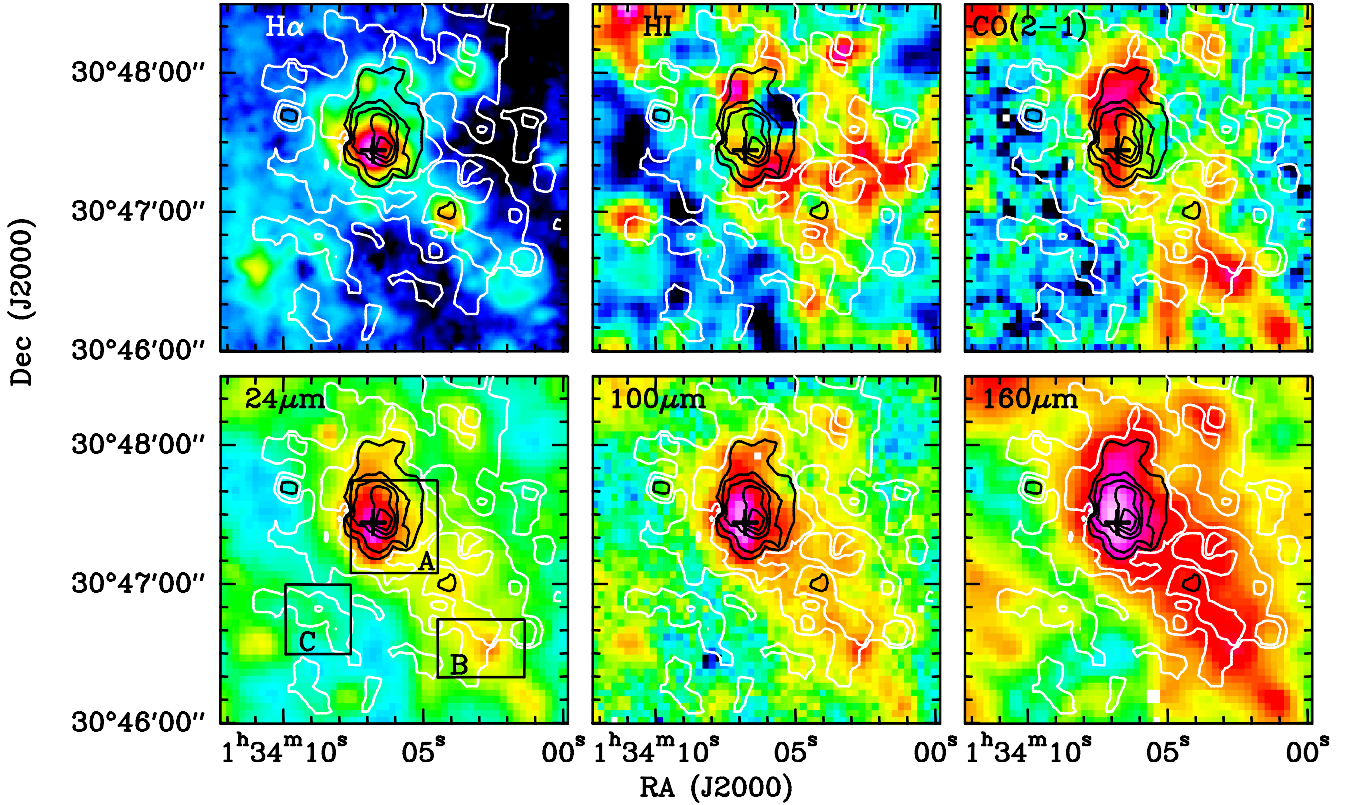
Fig. 5. Overlay of the Hα, H I, and ^{12}CO(2–1) emission and the dust continuum at 24 μm (MIPS), 100 μm and 160 μm (PACS) emission with contours of [C II] at 158 μm. The white and black contours are for intensities between 10–20% (in steps of 10%) and 30–90% (in steps of 15%) of the peak [C II] intensity of 1.18×10^{-4} erg s^{-1} cm^{-2} sr^{-1}. The beam sizes for Hα, H I, ^{12}CO(2–1), 24 μm, PACS 100 μm, PACS 160 μm, and ^{12}CO(2–1) observations are 1″, 12″, 12″, 6″, 6″.7, and 11″.4 respectively. The H I map is integrated between –280 km s^{-1} to –130 km s^{-1}. and the CO(2–1) map is integrated between –270 to –220 km s^{-1}. Marked in the 24 μm image (with black rectangles) are the regions selected for further analysis.

two ridges of CO emission, the arm running north-east to southwest, and a second ridge of emission running in the north-south direction. The northern part of this second ridge shows an interesting layering of emission: both [O I] and H I are slightly shifted towards the east relative to this CO ridge. However, there is a much weaker correspondence between [O I] and H I emission towards the east and north of the H II region.

3.2. HIFI spectroscopy of the Hα region

Figure 4 shows the velocity-resolved 158 μm [C II] spectrum observed with HIFI at the Hα peak position. In addition, we show the spectra of H I and the J = 2–1 transitions of CO and ^{13}CO. The HIFI and PACS integrated intensities agree very well. The [C II] integrated intensity of 15.6 K km s^{-1}, observed with HIFI corresponds to an intensity of 1.10×10^{-4} erg s^{-1} cm^{-2} sr^{-1}, which matches extremely well with the [C II] intensity observed with PACS, at the nearest PACS position, which is offset by only 3″.

All spectra are at a common resolution of ~12″, allowing for a detailed comparison. All spectral lines have a Gaussian shape. However, the line widths differ strikingly between the atomic material traced by H I, the [C II] line, and the molecular gas. The H I spectrum shows a *FWHM* of 16.5 km s^{-1}, that of [C II] is 13.3 km s^{-1}, while CO 2–1 shows a width of only 8 km s^{-1} (Table 2). We take this as an indication that the H I disk along the line of sight is much thicker than the molecular disk while the material traced by [C II] appears to lie in-between. In

Table 2. Parameters derived from Gaussian fits to spectra observed with HIFI, VLA, and IRAM 30 m, at the Hα peak position (Figs. 2 and 4), where θ_b indicates the half power beamwidth.

Line	θ_b ″	$\int T \, \mathrm{d}v$ K km s^{-1}	v_{cen} km s^{-1}	Δv km s^{-1}
[C II]	11	15.6 ± 0.5	-254.1 ± 0.1	12.9 ± 0.9
H I	11	1446.7 ± 44.1	-249.7 ± 0.2	16.5 ± 0.6
CO (1–0)	22	3.2 ± 0.2	-252.3 ± 0.2	7.5 ± 0.5
CO (2–1)	11	5.3 ± 0.1	-252.8 ± 0.1	7.9 ± 0.3
^{13}CO(1–0)	22	0.28 ± 0.02	-252.9 ± 0.2	5.8 ± 0.5
^{13}CO(2–1)	11	0.69 ± 0.06	-252.8 ± 0.3	6.2 ± 0.5

addition, we find that the lines are not centered at the same velocity. The HI line is shifted by +4.4 km s^{-1} relative to [C II], while the CO lines are shifted by +1.6 km s^{-1} relative to [C II], confirming that all three tracers trace different components of the ISM. The shifts are significant, as the error in the Doppler corrections are much smaller, for HIFI (Teyssier, priv. comm.) as for the other data.

On the basis of lower spectral resolution (6 km s^{-1}) optical spectroscopy of Hβ and [O III] emission lines, the velocity of the ionized gas is deduced to be shifted by –16.9 km s^{-1} with respect to the [C II] line, with a velocity dispersion of 11 km s^{-1} (Willner & Nelson-Patel 2002; Zaritsky et al. 1989). The optical spectroscopic data is however of much higher angular resolution (2–4″) that the *Herschel* data. A map of the emission lines originating solely from the ionized medium, which would allow us to
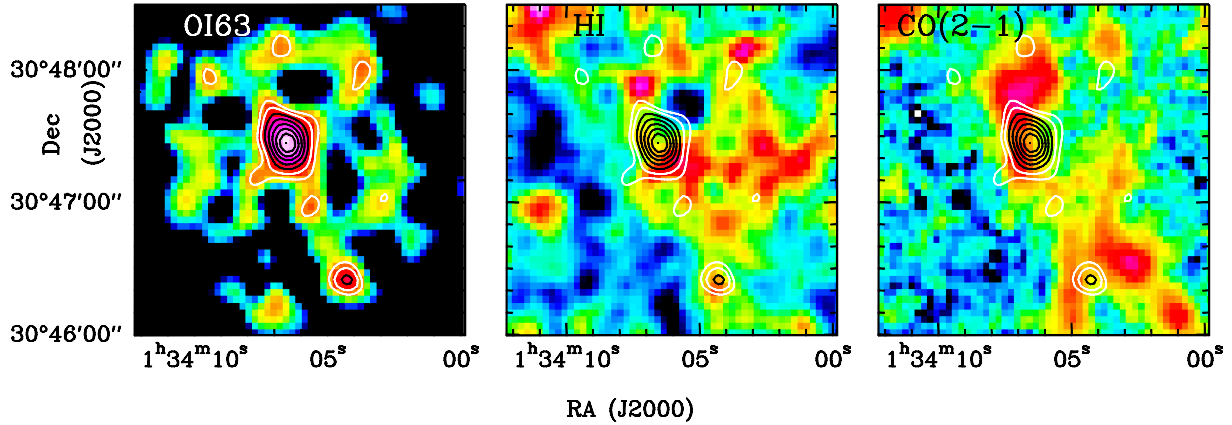
Fig. 6. Overlay of color plots of [O I] 63 µm, H I and ^{12}CO(2–1) emission with contours of [O I] at 63 µm. All plots are at a resolution of 12″. The white and black contours are for intensities in the range of 30–40% (in steps of 10%) and 50–100% (in steps of 10%) of peak [O I] intensity of 3.0×10^{-5} erg s^{-1} cm^{-2} sr^{-1}. Details of the H I and ^{12}CO(2–1) maps are identical to those in Fig. 5.

smooth these data to 12″ resolution for direct comparison with the other data, is not yet available. In Sect. 6.2, we use PDR models to show that about 20–30% of the observed [C II] stems from the ionized gas of the BCLMP 302 H II region.

In summary, we find a "layering" of the line-of-sight velocities tracing the different ISM components. The velocity increases from Hα to [C II], to CO, and to H I.

3.3. Detailed comparison of [C II] emission with other tracers

For a more quantitative estimate of the correspondence between the different tracers in which the spiral arm has been mapped, we created scatterplots of intensities of tracers such as Hα, ^{12}CO, H I, [O I] 63 µm, MIPS 24 µm, and PACS 100 µm as a function of the [C II] intensities (Fig. 7). We used intensities from all the maps that had been smoothed to a resolution of 12″ and gridded onto a 12″ grid. To identify any apparent trends in the emission we defined three sub-regions within the mapped region: region A corresponds to the H II region BCLMP 302 itself; region B corresponds to the south-western more quiescent part of the spiral arm, traced by e.g. the 100 µm continuum emission, and centered on a peak of CO emission; and region C lies outside of the prominent CO arm. These three sub-regions are marked by black rectangles in Fig. 5. A second H II region along the arm, lies just outside and to the north of the box defining the quiescent arm region. For the remainder of the paper, we always analyze and compare the results for these three sub-regions separately.

In the log-log scatter plots of Figure 7, we find that the Hα, [O I], and continuum emission at 24 µm and 100 µm show pronounced linear correlations with the [C II] emission within the H II region. In the region C, the intensities of the Hα emission and the continuum emission at 24 and 100 µm remain almost constant. The CO(2–1) intensity in the H II region (A) is only poorly correlated with the [C II] emission. In regions B and C, the CO(2–1) intensity shows no correlation with the [C II] intensity and has a large scatter. H I does not show any correlation with [C II].

A more quantitative analysis of the correlation between the different tracers and [C II], is obtained by calculating the correlation coefficient (r) (Table 3). For the entire region Hα and 24 µm and 100 µm intensities display a correlation close to 60% with the [C II] intensities. For the region A, the line intensities of Hα, [O I], 24 µm, and 100 µm are well correlated ($r > 0.75$) with [C II]. The Hα emission is strongly correlated with the [C II]

Table 3. Correlation coefficients for the scatter plots in Fig. 7.

Tracers	Correlation Coefficient			
	Entire Map	Region A	Region B	Region C
[C II]–Hα	0.60	0.93	0.66	0.30
[C II]–CO(2–1)	0.41	0.40	0.47	…
[C II]–H I	0.22	<0.1	<0.10	0.14
[C II]–[O I]	…	0.77	…	…
[C II]–F_{24}	0.61	0.86	0.66	0.41
[C II]–F_{100}	0.59	0.85	0.56	0.43

intensity also at the south-western arm position. The [O I]/[C II] intensity ratio measured primarily in the H II region varies between 0.1–0.4 and this variation is significantly larger than the estimated uncertainties.

4. [C II] as a tracer of star formation

In Fig. 8, we plot the SFR, estimated from the 24 µm MIPS data and the KPNO Hα data, as a function of the [C II] intensity. Positions within the selected regions A, B, and C are marked using different symbols and colors similar to Fig. 7. The SFR was calculated to be SFR = $[L(H\alpha) + 0.031L(24)] \times 5.35 \times 10^{-35}$ in $M_\odot$ yr^{-1}, where $L(H\alpha)$ is the Hα luminosity in Watt and $L(24)$ is defined as νL_ν at 24 µm in Watt (Calzetti et al. 2007). We assumed a Kroupa (2001) initial mass function with a constant SFR over 100 Myr. Here, we study the correlation on scales of 12″ corresponding to 50 pc. On these small scales, we may start to see a break-up of any tight correlations between the various tracers of the SFR.

Viewing all pixels, we find a steepening of the slope in the log-log plots from regions where both the SFR and [C II] are weak, to regions where both are strong. Towards the H II region (A), we find an almost linear relation between log(SFR) and log([C II]), with a good correlation, $r = 0.90$ and the fitted slope is 1.48 ± 0.26, i.e. the SFR goes as [C II] to the power 1.48. Region B shows a correlation coefficient of 0.64 and region C shows no correlation.

5. Energy balance in the spiral arm

Boquien et al. (in prep.) obtained a linear fit to the total infrared (TIR) luminosity as a function of the luminosity in the
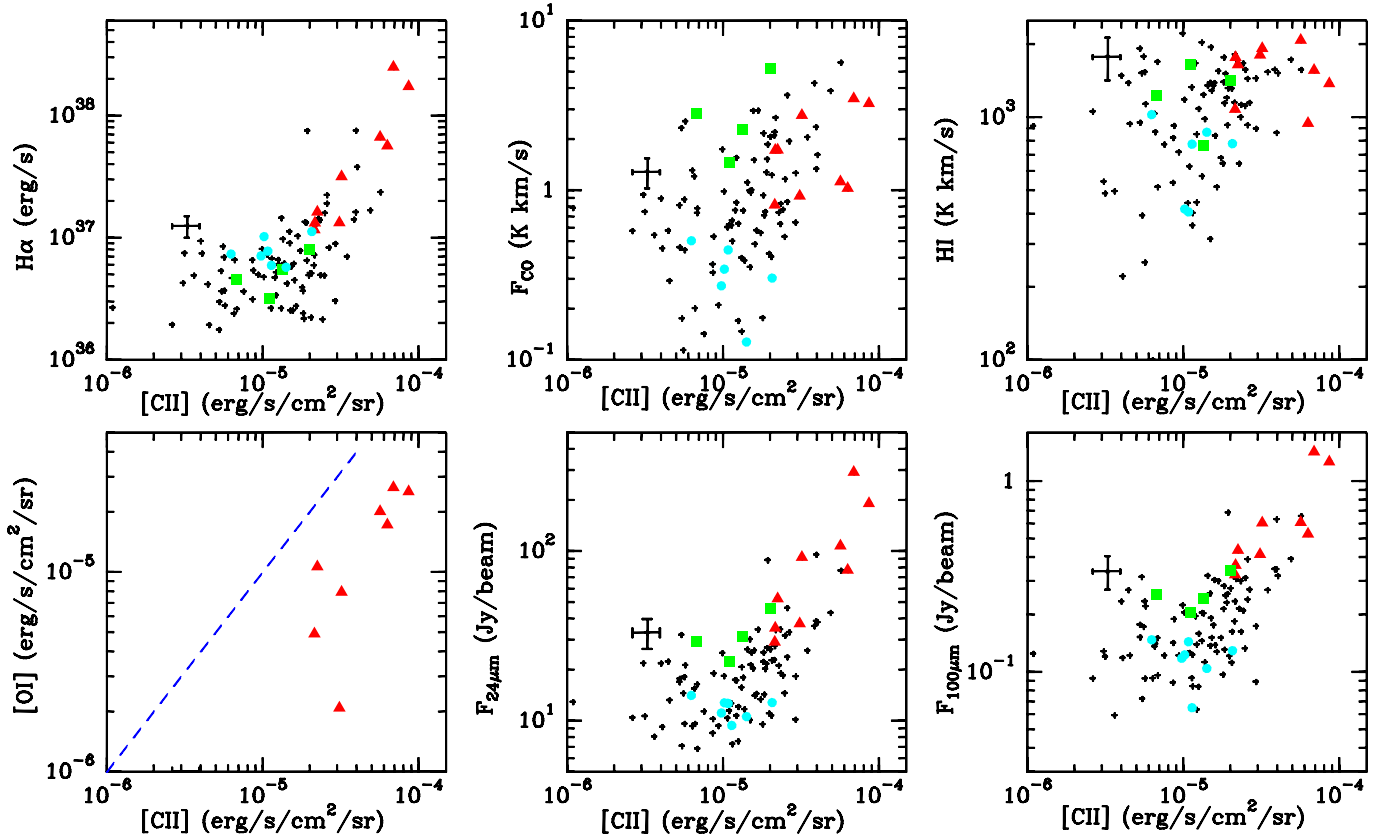
Fig. 7. Correlation of [C II] with Hα, ^{12}CO(2–1), H I, [O I] 63 μm, MIPS 24 μm, and PACS 100 μm. The black crosses mark all positions on a 6″ grid. The red triangles correspond to positions in region A, the green squares represent positions in region B, and the cyan filled circles correspond to positions in region C. All these regions are marked in the 24 μm map in Fig. 5. Errorbars corresponding to a 20% error in the plotted quantities along both axes are shown at one representative point in each panel. For [O I] 63 μm, only positions close to the H II region are used. The blue dashed line in the [C II]–[O I] scatter plot corresponds to equal intensities of the two tracers.

Table 4. Average values and their variation for the different tracers arising from the H II region, the spiral arm and the region C.

Tracer	Region A	Region B	Region C
[C II] (erg s^{-1} cm^{-2} sr^{-1})	$(4.51 \pm 2.30) \times 10^{-5}$	$(1.28 \pm 0.48) \times 10^{-5}$	$(1.19 \pm 0.42) \times 10^{-5}$
Hα (erg s^{-1})	$(7.1 \pm 6.9) \times 10^{37}$	$(5.3 \pm 1.8) \times 10^{36}$	$(7.95 \pm 1.93) \times 10^{36}$
CO (2–1) (K km s^{-1})	1.88 ± 0.98	2.95 ± 1.40	0.29 ± 0.14
H I ((K km s^{-1})	1597 ± 358	1267 ± 325	620 ± 309
[O I] (erg s^{-1} cm^{-2} sr^{-1})	$(1.28 \pm 0.09 \times 10^{-5}$	$\dots$	$\dots$
F_{24} (Jy beam^{-1})	101.9 ± 82.8	32.2 ± 8.6	11.9 ± 1.50
F_{100} (Jy beam^{-1})	0.66 ± 0.37	0.26 ± 0.05	0.12 ± 0.03

PACS 160 μm band for the entire M 33 galaxy. The TIR is the total infrared intensity, integrated between 1 μm and 1 mm. It is about a factor of two (Rubin et al. 2009) higher than the FIR continuum flux when the latter is integrated between 42.7 and 122 μm. Boquien et al. (in prep.) derived the TIR from fits of Draine et al. (2007) models to the MIPS, PACS, and SPIRE FIR data. They find a tight linear relation between the two quantities give by $\log L_{\text{TIR}} = a \times \log L_{160} + b$ with $a = 1.013 \pm 0.008$ and $b = 0.429 \pm 0.097$. We used this relation to derive the TIR intensity at each position of the mapped region, at a resolution of 12″. To check that this is a valid approach, we independently derived the TIR at individual positions by fitting a greybody to the MIPS, PACS, and SPIRE data, smoothed to a common resolution of 40″. The resulting TIR agrees to within 10% with the TIR derived from only the 160 μm band.

Figure 9 shows a scatterplot between TIR and [C II]. Positions corresponding to the selected sub-regions are indicated using different markers. We find that [C II] and TIR are tightly correlated with a correlation coefficient of 0.87 only in the H II region (A) with the fitted slope being 0.64 ± 0.14. The correlation coefficient in region B is 0.52 and in region C there is no correlation.

Incident FUV photons with energies high enough to eject electrons from dust grains ($h\nu > 6$ eV) heat the gas via these photoelectrons, with a typical efficiency of 0.1–1% (Hollenbach & Tielens 1997). Efficiency is defined as the energy input to the gas divided by the total energy of the FUV photons absorbed by dust grains. On the basis of ISO/LWS observations of a sample of galaxies, Malhotra et al. (2001) found that (a) more than 60% of the galaxies show $L_{\text{[CII]}}/L_{\text{FIR}} > 0.2\%$ and (b) $L_{\text{[CII]}}/L_{\text{FIR}}$ decreases with warmer FIR colors and increasing star formation activity, indicated by higher $L_{\text{FIR}}/L_{\text{B}}$ ratios, where L_{B} is the luminosity in the B band. We calculated the ratio of the intensities of [C II]/TIR, as a proxy for the heating
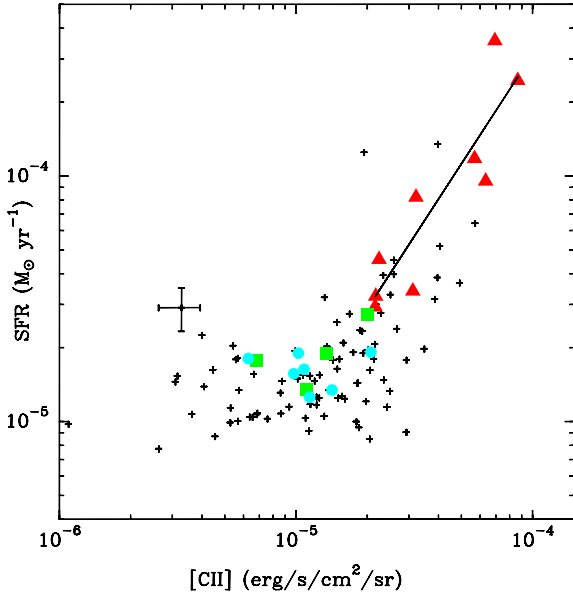
Fig. 8. Correlation of [C ii] intensities with SFR (derived from $24\,\mu m + H\alpha$). Red triangles correspond to positions in region A, the green squares represent positions in region B, and the cyan filled circles correspond to positions in region C. Each marker corresponds to one position on a 12″ grid. Details about the regions and points are identical to those in Fig. 7. The black straight line indicates the fits to the region A. The errorbar corresponds to an uncertainty of 20%.
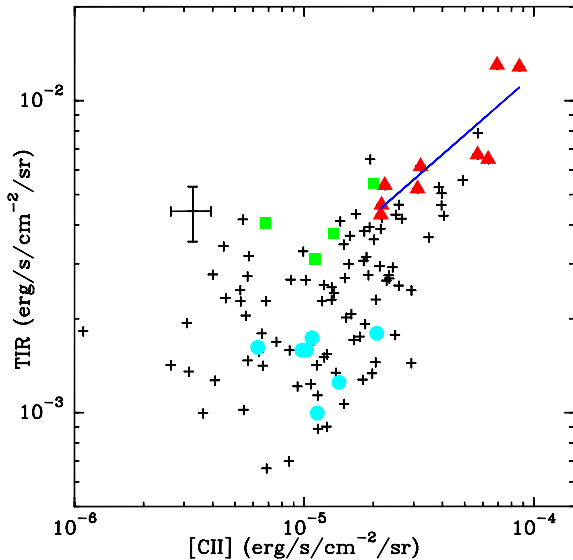
Fig. 9. Correlation plot of [C ii] and total infrared (TIR) intensities at a 12″ resolution and on a 12″ grid. Markers and the straight line are the same as in Fig. 7.

efficiency, and plotted it against with [C ii] intensities (Fig. 10). The heating efficiency vary by more than one order of magnitude within the $2' \times 2'$ region, between 0.07 and 1.5%. Considering an uncertainty of 20% in both the measured $160\,\mu m$ intensities and the [C ii] intensities, for the relation between the $160\,\mu m$ luminosity and the TIR luminosity mentioned earlier, we estimate the uncertainty in the [C ii]/TIR ratio to be ~30%. The observed variation in the [C ii]/TIR intensity ratios is significantly larger than the uncertainty we estimate from the [C ii] and $160\,\mu m$ intensities. For the H ii region A, we find heating efficiencies of between 0.2% and 1.0%. Regions B and C have efficiencies of between 0.15–0.4% and 0.4–1.2%. Within the H ii
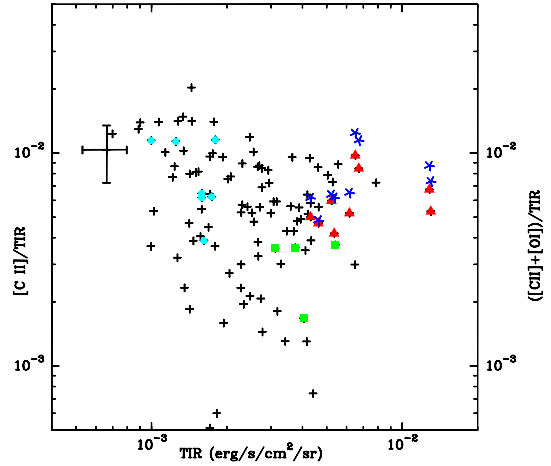
Fig. 10. Plot of [C ii]/TIR and ([C ii]+ [O i])/TIR (blue asterisks) in the H ii region as a function of the total infrared (TIR) intensities at a resolution of 12″ on a 6″ grid. The error bars denote 30% errors. Markers are the same as in Fig. 7.

region (A), the total heating efficiency, including the [O i] $63\,\mu m$ line, ([C ii]+[O i])/TIR, lies in the range 0.3–1.2% (Fig. 10). Outside the H ii region, reliable [O i] data is largely missing.

6. Modeling the PDR emission at the $H\alpha$ peak of BCLMP 302

6.1. Estimate of FUV from TIR

One of the key characteristics of PDRs is the FUV radiation field that heats the PDR. From energy considerations, the total infrared cooling emission is a measure of the irradiating FUV photon flux of the embedded OB stars. We estimate the FUV flux G_0 ($6\,eV < h\nu < 13.6\,eV$) impinging onto the cloud surfaces from the emerging total infrared intensities: $G_0 = 4\pi I_{FIR} = 4\pi\,0.5\,I_{TIR}$, where G_0 is in units of the Habing field $1.6 \times 10^{-3}\,erg\,s^{-1}\,cm^{-2}$ (Habing 1968) and the intensity of the far-infrared continuum between $42.5\,\mu m$ and $122.5\,\mu m$, I_{FIR}, is in units of $erg\,s^{-1}\,cm^{-2}\,sr^{-1}$. Following Tielens & Hollenbach (1985) our assumption of equal heating of grains by photons outside the FUV band contributes a factor of two to the expression for G_0. Further considering that the bolometric dust continuum intensity I_{TIR} is a factor of ~2 higher than I_{FIR} (Dale et al. 2001) gives rise to an additional factor of two.

At the $H\alpha$ peak position, the TIR intensity of $1.18 \times 10^{-2}\,erg\,s^{-1}\,cm^{-2}\,sr^{-1}$ translates into a FUV field of $G_0 = 46$ in Habing units. Outside the $H\alpha$ peak, the FUV field, estimated from the TIR, drops by more than one order of magnitude (cf. Fig. 9).

The FUV radiation leaking out of the clouds is measured using the GALEX UV data (Martin et al. 2005; Gil de Paz et al. 2007) to be $G_0 = 24$ for a 12″ aperture.

We thus find, that 66% of the FUV photons emitted by the OB stars of the H ii region are absorbed and re-radiated by the dust, and 34% leak out of the cloud, at the $H\alpha$ position. This is consistent with the FUV extinction derived from the $H\alpha$ and $24\,\mu m$ fluxes (Relaño & Kennicutt 2009) and the FUV/$H\alpha$ reddening curve (Calzetti 2001).

It is interesting to note that H ii regions observed in the LMC and other spiral galaxies by Oey & Kennicutt (1997) and Relaño et al. (2002) show that typically around 50% of the ionizing

Table 5. Properties of the H II region BCLMP 302.

Excitation parameter u	180 pc cm^{-2}	IK74
Radius r	39 pc	IK74
Mass	$10^5\,M_\odot$	IK74
rms electron density	6.2 cm^{-3}	IK74
Electron density n_e	100 cm^{-3}	R08
Ionization parameter U	-3.3	this paper
Effective temperature T_{eff}	38 000 K	this paper
Hα luminosity	2.2×10^{38} erg s^{-1}	KPNO map

Notes. As explained in the text, the value given for the electron density (n_e) is *assumed* to hold for BCLMP 302.

References. IK74 Israel & van der Kruit (1974), R08 Rubin et al. (2008).

Fig. 11. Comparison of line intensities and intensity ratios at the position of the Hα peak with plane-parallel constant density PDR models (Kaufman et al. 1999). Gray-scales show the estimated reduced χ^2. The horizontal line shows the FUV estimated from the total FIR intensity. The contours correspond to the intensities/ratios of different spectral lines (as shown in the labels). The [C II] intensity corresponds only to the estimated contribution (70% of the total) from the PDRs.

stellar radiation escape the H II regions, roughly similar to the fraction of 36% we find in BCLMP 302/M 33.
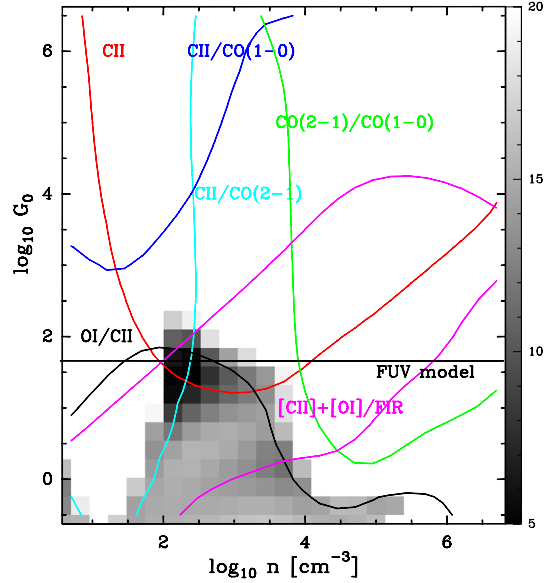
6.2. [C II] emission from the ionized gas

In Table 5 we present properties of the H II region BCLMP 302 compiled from the literature and also calculated thereof. These properties were used to estimate the fraction of [C II] emission contributed by this H II region using the model calculations of Abel et al. (2005); Abel (2006). These authors estimated the [C II] emission for a wide range of physical conditions in H II regions by varying their electron density n_e, ionization parameter U, and effective temperature T_{eff}.

The [C II] PACS map is centered on the bright H II region BCLMP302 (Boulesteix et al. 1974), which corresponds to the H II region No. 53 in the M 33 catalog of Israel & van der Kruit (1974, IK74). Using the measured radio flux and the formula $u(\mathrm{pc\,cm^{-2}}) = 13.5(S/\mathrm{f.u.})^{1/3}(D/\mathrm{kpc})^{2/3}$ (Israel et al. 1973), IK74 estimate the excitation parameter $u = 180$ pc cm^{-2} for a distance of 720 kpc. IK74 also derive an rms electron density of 6.2 cm^{-3}, and estimate the radius r of the H II region to be 38.5 pc. We did not correct these results for the more accurately known distance, as it does not affect our conclusions. For an electron temperature T_e of 10 000 K, Panagia (1973) expresses the excitation parameter as $u(\mathrm{pc\,cm^{-2}}) = 2.2 \times 10^{-19}\left[N(L)(\beta - \beta_1)^{-1}\right]^{1/3}$, where $(\beta{-}\beta_1)$ is the recombination rate to the excited levels of hydrogen in units of cm^3 s^{-1}. Thus, we get for the total flux of ionizing photons $N(L) = 4.6 \times 10^{43}\,u^3$ s^{-1}. Using the above values of the parameters, the dimensionless ionization parameter U was derived via $U = N(L)/(c\,4\pi r^2\,n_{H+})$ (Evans & Dopita 1985; Morisset 2004).

The rms electron density derived by IK74, provides only a lower limit to the true electron density, and observations of for instance the [S II] doublet at 6754 Å would be required to perform a direct estimate. Rubin et al. (2008) observed 25 H II regions in M 33 using *Spitzer*-IRS, and concluded that their electron densities are ~100 cm^{-3}. Since there is no apparent reason for the n_e in BCLMP 302 to be significantly different, we assume $n_e = 100$ cm^{-3}. Hence, with $n_{H+} = n_e$, we estimate log $U = -3.3$ (Table 5).

The observed ratio of double to single ionized nitrogen, [N III] 57 μm/[N II] 122 μm, at the Hα position (Table 1), indicates an effective temperature of the ionizing stars of about 38 000 K (Rubin et al. 1994).

From the model calculations of Abel (2006, Fig. 5), we estimate the fraction of [C II] emission from the BCLMP 302

H II region. The [C II] fraction increases with decresing electron density, but is only weakly dependent on the ionization parameter and the stellar continuum model. Depending on the model, the resulting fraction varies slightly, ~20−30%. The fraction would drop to about 10%, for an electron density of 10^3 cm^{-3}.

Observations of the [N II] 205 μm line, in addition to the 122 μm line would allow us to estimate more accurately the electron density of the H II region. The model calculations and observations compiled by Abel (2006) demonstrate that the [C II] intensities originating from H II regions and the intensities of the [N II] 205 μm line are tightly correlated. Abel (2006) find $\mathrm{Log}\left[I_{H+}^{C+}\right] = 0.937\mathrm{Log}\left[I_{H+}^{NII}\right] + 0.689$ (erg cm^{-2} s^{-1}). Assuming that 30% of the [C II] emission stems from the BCLMP 302 H II region at the Hα peak position, we estimate a [N II] 205 μm intensity of ~3.6×10^{-6} erg s^{-1} cm^{-2} sr^{-1} (cf. Table 1), corresponding to 3×10^{-18} W m^{-2}. The expected [N II] 205 μm intensity is a factor of three below the estimated rms of our PACS observations, hence is consistent with the non-detection. Using the detected [N II] 122 μm line and the predicted [N II] 205 μm intensity from above, the [N II] 122 μm/[N II] 205 μm ratio is 2.8; this corresponds to an n_e of 10^2 cm^{-3} (Abel et al. 2005, Fig. 22), which is consistent with the n_e assumed by us for the above calculations.

6.3. Comparison with PDR models

Here we investigate whether the FIR and millimeter lines, together with the TIR, observed towards the Hα peak, can be consistently explained in terms of emission from the PDRs at the surfaces of the molecular clouds. We use the line and total infrared continuum intensities at a common resolution of 12″.

At the position of the Hα peak, we observe the following intensity ratios on the erg scale (cf. Table 6) [O I]/[C II] = 0.35, [C II]/CO(1−0) = 1.1 × 10^4, [C II]/CO(2−1) = 1263, ([C II]+ [O I])/TIR = 9.6×10^{-3}, and CO(2−1)/CO(1−0) = 8.8. Comparing

Table 6. Input to the PDR model for the HIFI position.

Tracer	Intensity
[C II]*	8.4×10^{-5}
[O I]	3.0×10^{-5}
CO (1–0)**	7.5×10^{-9}
CO (2–1)	6.7×10^{-8}
TIR	1.18×10^{-2}

Notes. All intensities are in units of erg s^{-1} cm^{-2} sr^{-1}. (*) The observed [C II] intensities was multiplied by 0.7, assuming that 30% of the emission stems from the H II region. (**) The CO 1–0 data at 22″ resolution were multiplied by the beam-filling factor 1.5, estimated by smoothing the 2–1 data from 11″ to 22″ resolution.

all ratios with the PDR model of Kaufman et al. (1999) (Fig. 11), we find a best-fitting solution near a FUV field of $G_0 = 32$ in units of the Habing field and a density of 320 cm^{-3}. The fitted FUV field agrees rather well with the FUV field of $G_0 = 46$ (in Habing units) estimated from the TIR continuum. The corresponding reduced χ^2 was estimated assuming an error of 30% in the observed intensity ratios. The reduced χ^2 is defined as $\chi^2 = 1/(n-2)(\sum_{i=0}^{n}(I_i^{obs} - I_i^{model})^2/\sigma_i^2)$, where $(n-2)$ is the number of degrees of freedom with n being the number of observed quantities used for the fitting and I denotes either integrated intensities or ratios of integrated intensities. We find the minimum value of χ^2 to be 4.4, indicating that the fit is unsatisfactory. The fitted density indeed seems rather low, given the high critical densities of the [C II] and in particular also of the [O I] line. On the other hand, the observed [O I]/[C II] ratio, is consistent with the low density solution. The ratios involving the CO lines, deviate from this solution. For instance, the CO 2–1/1–0 ratio together with the derived FUV, indicates a higher density of about 10^4 cm^{-3}. Using line ratios to compare with the PDR model, allows us to ignore beam-filling effects, to first order. We note that the absolute [C II] intensity, reduced by the fraction of 30% stemming from the H II region, agrees well with the best-fitting solution, indicating a [C II] beam-filling factor of about 1.

The rather poor fit of the intensity ratios towards the Hα peak illustrates the shortcomings of a plane-parallel single density PDR model. First tests using the KOSMA-τ PDR models of Röllig et al. (2006) of spherical clumps with density gradients provide more satisfactory reproduction of the observations. This indicates that there are strong density gradients along the line of sight. In a second paper, we shall include new HIFI [C II] data along two cuts through the BCLMP 302 region and explore detailed PDR models, which include the effects of geometry and sub-solar metallicity.

7. Discussion

Mapping observations of the northern inner arm of M 33 at an unprecedented spatial resolution of 50 pc, we have investigated the distribution of the various components of the interstellar medium and their contribution to the [C II] emission. The [C II] spectral line at 158 μm is one of the major cooling lines of the interstellar gas. Thus, irrespective of whether hydrogen is atomic or molecular, the [C II] line emission is expected to be strong wherever there is warm and photodissociated gas. We have identified emission towards the H II region as well as from the spiral arm seen in the continuum, and from a region outside the well-

defined spiral arm. The [C II] emission is strongly correlated with the Hα and dust continuum emission, while there is little correlation with CO, and even less with H I. This suggests that the cold neutral medium (CNM; Wolfire et al. 1995) does not contribute significantly to the [C II] emission in the BCLMP 302 region. Langer et al. (2010) found a similarly poor correlation between [C II] and H I emission in a sample of 29 diffuse clouds using HIFI. The lack of correlation between [C II] and CO found in BCLMP 302, may indicate that significant parts of the molecular gas are not traced by CO because it is photo-dissociated in the low-metallicity environment of M 33. This interpretation is consistent with both theoretical models developed by Bolatto et al. (1999) and observational studies of both diffuse clouds in the Milky Way by Langer et al. (2010), and dwarf galaxies by Madden et al. (2011).

The comparison of the first velocity-resolved [C II] spectrum of M 33 (at the Hα peak of BCLMP 302) with CO line profiles show that the [C II] profile is much broader, by a factor of ~1.6, and slightly shifted in velocity, by ~1.6 km s^{-1}. Relative to the H I line, at the same angular resolution, the [C II] line is narrower by a factor ~1.3 and shifted by ~4.4 km s^{-1}. These findings indicate that the [C II] line is not completely mixed with the CO emitting gas, but rather traces an additional more turbulent outer layer of gas with a slightly different systemic velocities, which is associated with the ionized gas.

Interestingly, [C II] HIFI observations of Galactic star-forming regions (Ossenkopf et al. 2010; Joblin et al. 2010) also show broadened and slightly shifted [C II] line profiles relative to CO.

The two major cooling lines of PDRs are the [O I] line at 63 μm and the [C II] 158 μm line. The intensity ratios [OI]/[CII] and ([OI]+[CII]) versus the TIR continuum, have been used extensively to estimate the density and FUV field of the emitting regions. Using ISO/LWS, Higdon et al. (2003) observed the far-infrared spectra of the nucleus and six giant H II regions in M 33, not including BCLMP 302, but including NGC 604, IC 142, and NGC 595 shown in Fig. 1. The 70″ ISO/LWS beam corresponds to 285 pc hence samples a mixture of the different ISM phases. They find [O I]/[C II] line ratios in the range 0.7 to 1.3, similar to the range of values found at the center and spiral arm positions of M 83 and M 51 (Kramer et al. 2005). Towards the H II region BCLMP 302 in the northern inner arm of M 33, we measure much smaller [O I]/[C II] ratios in the range 0.1–0.4. These ratios lie towards the lower end of the values found by Malhotra et al. (2001) in their ISO/LWS study of the unresolved emission of 60 galaxies who find values between ~0.2 and 2. Similarly small values as low as 0.16 are found e.g. in the Galactic star-forming regions DR 21 and W3 IRS5 (Jakob et al. 2007; Kramer et al. 2004). Comparison with the PDR models of Kaufman et al. (1999, Fig. 4) and Röllig et al. (2006) show that the [O I] 63 μm line becomes stronger than the [C II] emission in regions of high densities of more than about 10^4 cm^{-3}. At the Hα peak position in BCLMP 302, we observed a ratio of 0.4, after correcting [C II] for the contribution from the ionized gas. This ratio indicates lower densities and a FUV field of less than about $100 G_0$ (cf. Fig. 11). Still lower ratios would correspond to weaker impinging FUV fields.

The ratio of [O I] +[C II] emission to the FIR continuum flux, is a good measure of the total cooling of the gas relative to the cooling of the dust, reflecting the ratio of FUV energy heating the gas to the FUV energy heating the grains, hence the grain heating efficiency, i.e. the efficiency of the photo-electric (PE) effect (Rubin et al. 2009). Efficiencies of up to about 5% are still consistent with FUV heating, i.e. with emission from PDRs
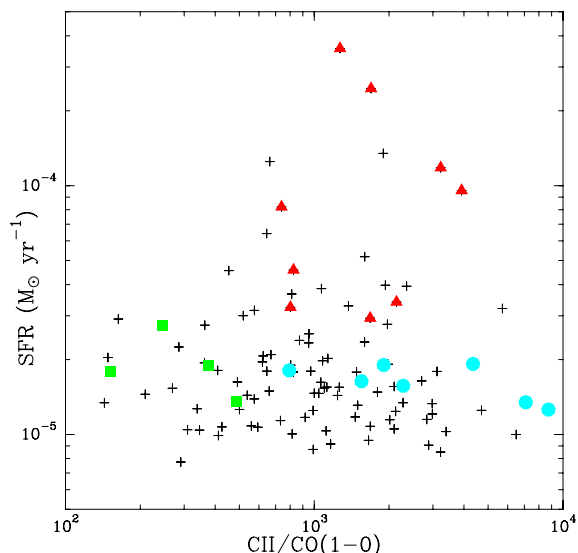
Fig. 12. Star formation rate (SFR) versus the [C II]/CO(1–0) intensity ratio. Markers are the same as in Fig. 7.

(Bakes & Tielens 1994; Kaufman et al. 1999). The PE heating efficiency is a function of FUV field, electron density, and temperature. A high FUV field leads to a large fraction of ionized dust particles, lowering the efficiency. On the other hand, low metallicities naturally lead to higher efficiencies as e.g. the PDRs become larger when the dust attenuation is lower (Rubin et al. 2009).

Higdon et al. (2003) compared the [O I]+[C II] emission with the FIR(LWS) continuum integrated between 43 and 197 μm, and obtained ratios of 0.2% to 0.7%, corresponding to 0.1 to 0.35% corresponding to an approximate FIR/TIR conversion factor of two (Dale et al. 2001; Rubin et al. 2009). Towards the $2' \times 2'$ region presented here, the [C II]/TIR ratio varies by more than a factor of a ten between 0.07% and 1.5%. Extragalactic observations at resolutions of 1 kpc or more, find efficiencies of only up to ~0.3% (Kramer et al. 2005; Malhotra et al. 2001). The observations of M 31 by Rodriguez-Fernandez et al. (2006) with ISO/LWS at ~300 pc resolution, also yield high efficiencies of up to 2%. Rubin et al. (2009) analyzed BICE [C II] maps of the LMC at 225 pc resolution, and find efficiencies of upto 4% in this low metallicity environment. The mean values found in the LMC are however much lower: 0.8% in the diffuse regions, dropping to ~0.4% in the SF regions. A similar variation was found in the Galactic plane observations by Nakagawa et al. (1998). Heating efficiencies observed in the Milky Way span about two orders of magnitude. Habart et al. (2001) observed efficiencies as high as 3% in the low-UV irradiated Galactic PDR L1721, whereas Vastel et al. (2001) also using ISO/LWS fluxes of [C II] and [O I], found a very low heating efficiency of 0.01% in W49N. The global value for the Milky Way from COBE observations is ~0.15% (Wright et al. 1991). The averages over the entire galaxies observed by e.g. Malhotra et al. (2001), are dominated by bright emission from the nuclei where the SFR and the FUV fields are strong, hence lowering the photo-electric heating efficiencies.

Unresolved observations of external galaxies have led to the discovery of a tight correlation between CO and [C II] emission. This was initially seen by Stacey et al. (1991) with the KAO, and subsequently supported by ISO/LWS observations. However, on spatial scales of 50 pc we do not detect such a tight correlation in BCLMP 302. This lack of correlation be-

tween CO and [C II] emission is already seen in the maps of spiral arms in M 31 at ~300 pc resolution (Rodriguez-Fernandez et al. 2006). As summarized by them, the [C II]/CO(1–0) ratio varies from ~1300 in galactic disks to about 6000 in starbursts and to about 23 000 in the LMC. In BCLMP 302/M 33, we find that the [C II]/CO(1–0) ratio varies between 200 and 6000, with the H II region having values in the range 800–5000 (Fig. 12). The region C shows large values of the [C II]/CO(1–0) intensity ratios as CO is hardly detected. Thus, while the [C II]/CO(1–0) intensity ratios are higher for regions with high SFRs, there is no marked correlation between the two quantities on scales smaller about 300 pc. The tight correlation between [C II] and CO emission breaks down on scales for which the spiral arms of galaxies are resolved.

References

Abel, N. P. 2006, MNRAS, 368, 1949
Abel, N. P., Ferland, G. J., Shaw, G., & van Hoof, P. A. M. 2005, ApJS, 161, 65
Asplund, M., Grevesse, N., Sauval, A. J., & Scott, P. 2009, ARA&A, 47, 481
Bakes, E. L. O., & Tielens, A. G. G. M. 1994, ApJ, 427, 822
Beirão, P., Armus, L., Appleton, P. N., et al. 2010, A&A, 518, L60
Bolatto, A. D., Jackson, J. M., & Ingalls, J. G. 1999, ApJ, 513, 275
Boquien, M., Calzetti, D., Kramer, C., et al. 2010, A&A, 518, L70
Boulesteix, J., Courtes, G., Laval, A., Monnet, G., & Petit, H. 1974, A&A, 37, 33
Calzetti, D. 2001, PASP, 113, 1449
Calzetti, D., Kennicutt, R. C., Engelbracht, C. W., et al. 2007, ApJ, 666, 870
Contursi, A., Kaufman, M. J., Helou, G., et al. 2002, AJ, 124, 751
Cooksy, A. L., Blake, G. A., & Saykally, J. 1986, ApJ, 305, 89
Crawford, M. K., Genzel, R., Townes, C. H., & Watson, D. M. 1985, ApJ, 291, 755
Dale, D. A., Helou, G., Contursi, A., Silbermann, N. A., & Kolhatkar, S. 2001, ApJ, 549, 215
Draine, B. T., & Li, A. 2007, ApJ, 657, 810
Evans, I. N., & Dopita, M. A. 1985, ApJS, 58, 125
Ferland, G. J., Korista, K. T., Verner, D. A., et al. 1998, PASP, 110, 761
Freedman, W. L., Wilson, C. D., & Madore, B. F. 1991, ApJ, 372, 455
Gil de Paz, A., Boissier, S., Madore, B. F., et al. 2007, ApJS, 173, 185
Gratier, P., Braine, J., Rodriguez-Fernandez, N. J., et al. 2010, A&A, 522, A3
Gry, C., Swinyard, B., Harwood, A., et al. 2003, The ISO Handbook, Vol. III – LWS – The Long Wavelength Spectrometer Version 2.1, June, 2003, Series, ed. T. G. Mueller, J. A. D. L. Blommaert, & P. Garcia-Lario, ESA SP-1262, ISSN No. 0379-6566, European Space Agency
Habart, E., Verstraete, L., Boulanger, F., et al. 2001, A&A, 373, 702
Habing, H. J. 1968, Bull. Astron. Inst. Netherlands, 19, 421
Heiles, C. 1994, ApJ, 436, 720
Higdon, S. J. U., Higdon, J. L., van der Hulst, J. M., & Stacey, G. J. 2003, ApJ, 592, 161
Hollenbach, D. J., & Tielens, A. G. G. M. 1997, ARA&A, 35, 179
Hoopes, C. G., & Walterbos, R. A. M. 2000, ApJ, 541, 597
Israel, F. P., & van der Kruit, P. C. 1974, A&A, 32, 363 (IK74)
Israel, F. P., Habing, H. J., & de Jong, T. 1973, A&A, 27, 143
Israel, F. P., Maloney, P. R., Geis, N., et al. 1996, ApJ, 465, 738
Jakob, H., Kramer, C., Simon, R., et al. 2007, A&A, 461, 999
Joblin, C., Pilleri, P., Montillaud, J., et al. 2010, A&A, 521, L25
Kaufman, M. J., Wolfire, M. G., Hollenbach, D. J., & Luhman, M. L. 1999, ApJ, 527, 795
Kramer, C., Jakob, H., Mookerjea, B., et al. 2004, A&A, 424, 887
Kramer, C., Mookerjea, B., Bayet, E., et al. 2005, A&A, 441, 961
Kramer, C., Buchbender, C., Xilouris, E. M., et al. 2010, A&A, 518, L67
Kroupa, P. 2001, MNRAS, 322, 231
Langer, W. D., Velusamy, T., Pineda, J. L., et al. 2010, A&A, 521, L17
Madden, S. C., Geis, N., Genzel, R., et al. 1993, ApJ, 407, 579
Madden, S. C., Galametz, M., Cormier, D., et al. 2011 [arXiv:1105.1006]
Malhotra, S., Kaufman, M. J., Hollenbach, D., et al. 2001, ApJ, 561, 766
Martin, D. C., Fanson, J., Schiminovich, D., et al. 2005, ApJ, 619, L1
Morisset, C. 2004, ApJ, 601, 858
Nakagawa, T., Yui, Y. Y., Doi, Y., et al. 1998, ApJ, 115, 259
Nikola, T., Geis, N., Herrmann, F., et al. 2001, ApJ, 561, 203
Oey, M. S., & Kennicutt, R. C., Jr. 1997, MNRAS, 291, 827
Olberg, M. 2010, Beam observations towards Mars, Technical Note, ICC, Vers. 1.1, 2010-11-17
Ossenkopf, V., Röllig, M., Simon, R., et al. 2010, A&A, 518, L79

Ott, S. 2010, in Astronomical Data analysis Software and Systems XIX, ed. Y. Mizumoto, K. I. Morita, & M. Ohishi, ASP Conf. Ser., in press

Panagia, N. 1973, AJ, 78, 929

Poglitsch, A., Waelkens, C., Geis, N., et al. 2010, A&A, 518, L2

Regan, M. W., & Vogel, S. N. 1994, ApJ, 434, 536

Relaño, M., & Kennicutt, R. C. 2009, ApJ, 699, 1125

Relaño, M., Peimbert, M., & Beckman, J. 2002, ApJ, 564, 704

Rodriguez-Fernandez, N. J., Braine, J., Brouillet, N., & Combes, F. 2006, A&A, 453, 77

Röllig, M., Ossenkopf, V., Jeyakumar, S., Stutzki, J., & Sternberg, A. 2006, A&A, 451, 917

Röllig, M., Abel, N. P., Bell, T., et al. 2007, A&A, 26, 467

Rubin, R. H., Simpson, J. P., Lord, S. D., et al. 1994, ApJ, 420, 772

Rubin, R. H., Simpson, J. P., Colgan, S. W. J., et al. 2008, MNRAS, 387, 45 (R08)

Rubin, D., Hony, S., Madden, S. C., et al. 2009, A&A, 494, 647

Stacey, G. J., Geis, N., Genzel, R., et al. 1991, ApJ, 373, 423

Tabatabaei, F. S., Beck, R., Krause, M., et al. 2007, A&A, 466, 509

Tielens, A. G. G. M., & Hollenbach, D. 1985, ApJ, 291, 722

Vastel, C., Spaans, M., Ceccarelli, C., Tielens, A. G. G. M., & Caux, E. 2001, A&A, 376, 1064

Verley, S., Relaño, M., Kramer, C., et al. 2010, A&A, 518, L68

Willner, S. P., & Nelson-Patel, K. 2002, ApJ, 568, 679

Wolfire, M. G., Tielens, A. G. G. M., & Hollenbach, D. 1990, ApJ, 358, 116

Wolfire, M. G., Hollenbach, D., McKee, C. F., Tielens, A. G. G. M., & Bakes, E. L. O. 1995, ApJ, 443, 152

Wright, E. L., Mather, J. C., Bennett, C. L., et al. 1991, ApJ, 381, 200

Zaritsky, D., Olszewski, E. W., Schommer, R. A., Peterson, R. C., & Aaronson, M. 1989, ApJ, 345, 759